An Isotropic Minimal Path Based Framework for Segmentation and Quantification of Vascular Networks

Emmanuel Cohen[1,2], Laurent D. Cohen[1], Thomas Deffieux[2], and Mickael Tanter[2]

[1] CEREMADE, PSL Research University, Université Paris Dauphine, CNRS, UMR 7534, 75016 Paris, France
[2] Institut Langevin, PSL Research University, ESPCI ParisTech, CNRS, UMR 7587, INSERM U979, 75005 Paris, France, `emmanuel.cohen@espci.fr`

Abstract. Minimal path approaches for image analysis aim to extract curves minimizing an energy functional. The energy of a path corresponds to its weighted curve length according to a relevant metric function. In this study, we design a binary isotropic metric model with the use of a Hessian-based vascular enhancement filter in order to extract geometrical features from vascular networks. We introduce a constrained keypoint search method able to extract subpixel vessel centrelines, diameters and bifurcations. Experiments on retinal images demonstrated that the proposed framework achieves similar even better segmentation performances as compared with methods using more sophisticated metric designs.

1 Introduction

Vascular networks in the human body own anatomical characteristics that are crucial to analyse for diverse purposes, e.g. in biology for a better understanding of the vascular architecture, or in medicine for the diagnosis of many diseases such as vessel tortuosity based analyses [5, 15]. In Cohen et al. [9], we also showed that the vascular anatomy represent a useful positioning landmark for neuronavigation and image registration. Therefore, in this paper, we aim to develop numerical methods for accurately extracting geometrical features from the vascular data, such as vessel centrelines, diameters, bifurcations, etc.

Geodesic methods for minimal path extraction in images have widely demonstrated their worth [10, 21], in particular to extract path from tubular structures for medical applications [13, 4]. A minimal path or *geodesic* joining two points in an image is a curve that globally minimizes a well chosen energy among all curves joining these two points. The energy of a path corresponds to its curve length weighted by a potential or metric function. The metric assigns to every pixel a scalar weight (isotropic case) by privileging pixels of interest like those from tubular-vessel structures by assigning them low weights. Thus, minimal paths preferably follows vessel structures of the image.

The choice of the metric represents a major issue. Several authors have already proposed different types of metrics according to the type of processed images as summarized in [21]. Isotropic intensity-based metrics favour salient pixels according to their intensity and position only. As a consequence, minimal paths can deviate and miss some vessels or take a shortcut generally due to image noise. To overcome this problem, the metric must take into account the geometry of vessels in order to better discriminate them. Thus, Benmansour and Cohen [4] introduced an anisotropic metric design based on the optimally oriented flux (OOF) filter [18] to incorporate the local orientation of vessels.

Another important issue is the way to extract the entire vascular tree. Benmansour and Cohen [3] proposed a minimal path method with keypoints detection (MPWKD) all along the curves of interest given a single source (start) point. Instead of collecting many pairs of source and endpoints, a unique path grows iteratively through the entire vascular network. However, the method suffers from detection of outlier keypoints or paths due to the isotropy of the metric and the simplicity of the stopping criterion. An improvement of the method is proposed in [7] with the use of an OOF based anisotropic metric and a more specific stopping criterion.

Beyond the problem of extracting relevant minimal paths, methods for quantification of vascular networks require also the paths to be centred enabling for instance evaluation of vessel tortuosity, and furthermore a local estimation of vessel diameters. In Li et al. [19], they solved the minimal path problem by adding an extra dimension to the classical Fast Marching scheme [24]. They characterized a point by its euclidean coordinates added by the radius at this point. This allows to extract both the centred vessel paths and the corresponding diameters. Yet, despite the accuracy of the method, this one dimension higher scheme increases computing times, a serious drawback regarding real time applications.

In this paper, we propose a minimal path based method to extract entire vascular trees with accurate centrelines, diameters, and bifurcations, that competes with the above state of the art while keeping an isotropic metric and a classical Fast Marching scheme. This prevents from dealing with the problem of high anisotropy ratios [20], and the numerical scheme preserves its classical dimension.

Instead of incorporating the vessel orientation inside an anisotropic metric, we propose to use an isotropic binary metric classifying pixels as vessel or non-vessel. As a consequence, the extracted minimal paths are necessary constrained to follow a priori segmented vascular structures. This binary metric can be simply obtained by thresholding a *vesselness* map i.e. the response of a vascular enhancement filter. We could use any successful filter such as OOF or Hessian-based methods [14]. We chose the most recent and efficient Hessian-based filter introduced by Jerman et al. [16]. To centre the extracted paths and deduce the corresponding diameters, we constrained the MPWKD method to detect only centred keypoints and paths by using a pre-computing distance-to-boundary map. At the end, we get a complete graph representation of vascular networks with subpixel precise centred vessel paths, local diameters, bifurcations, and taking into account cycles or closed curves in the graph.

The paper is organized as follows. In Section 2, we recall some backgrounds on the minimal path extraction method. Section 3 describes the proposed framework. In Section 4, we show some experimental results on 2D retinal images from the DRIVE database [26]. Conclusion and future works are given in Section 5.

2 Background

This study deals with 2D images for simplicity of visualization and validation of the results but one can straightforwardly extend the method to 3D e.g. on the basis of [13, 16]. Let Ω be a closed subset of $\mathbb{N}^2$ and $I : \Omega \to [0,1]$ a 2D image .

2.1 Minimal Path Extraction

Given an isotropic (scalar) potential or metric function $\mathcal{P} : \Omega \to \mathbb{R}$, the minimal path γ^* joining a source point $s \in \Omega$ to an endpoint $e \in \Omega$ is the global minimizer of the following energy

$$\mathcal{E}(\gamma) = \int_0^1 \mathcal{P}(\gamma(t), \gamma'(t))dt \tag{1}$$

among all smooth curves $\gamma : [0,1] \to \Omega$ joining $\gamma(0) = s$ to $\gamma(1) = e$. To solve this minimization problem, let define the geodesic distance map $\mathcal{U}_S : \Omega \to \mathbb{R}$ for any set S of source points by

$$\mathcal{U}_S(x) = \min_{\substack{\gamma(0)\in S \\ \gamma(1)=x}} \mathcal{E}(\gamma). \tag{2}$$

Inspired from works on the viscosity solutions of Hamilton-Jacobi equations [11, 22], Cohen and Kimmel [10] noticed that $\mathcal{U}_S$ satisfies the Eikonal equation and used the Fast Marching numerical scheme introduced by Sethian [23] to solve it. The Fast Marching is a front propagation approach computing iteratively the values of $\mathcal{U}_S$ in increasing order from the source points verifying

$$\mathcal{U}_S(s) = 0 \ , \ \forall s \in S. \tag{3}$$

Thus, γ^* can be easily extracted by performing a gradient descent on $\mathcal{U}_S$ from e to s.

To get a more accurate numerical solution for $\mathcal{U}_S$, we prefer to use the numerical scheme introduced by Tsitsiklis [27] also detailed in [17].

2.2 Automatic Keypoint Detection

In the previous section, the user needs to provide source and endpoints. When dealing with complex tubular structures with many bifurcations like vascular networks, we need an automatic procedure. The Benmansour and Cohen [3] method (MPWKD) has the benefit to extract automatically from one single source point several successive minimal paths following the entire tree structure. This is achieved by iteratively detecting keypoints along the tree and at each iteration tracing back to the previous keypoint by gradient descent on $\mathcal{U}_S$ (see also [19]).

The criterion to detect a keypoint is based on the computation of the euclidean distance map $\mathcal{L}_S$ in parallel with the geodesic distance map. Starting from the source points $S = \{s_0, ..., s_{n_S}\}$ with $\mathcal{U}_S(s) = 0$ and $\mathcal{L}_S(s) = 0$ for all $s \in S$, the front propagates according to the Fast Marching algorithm with metrics $\mathcal{P}$ and $\tilde{\mathcal{P}} = 1$ respectively for $\mathcal{U}_S$ and $\mathcal{L}_S$, until a point p_0 satisfying $\mathcal{L}_S(p_0) \geq \lambda$ is designated as a new keypoint. The crucial part of the algorithm is now to update $\mathcal{U}_S(p_0) = 0$ and $\mathcal{L}_S(p_0) = 0$ so that p_0 becomes also a new source point and $S \leftarrow S \cup \{p_0\}$. This process is iterated to obtain a set of keypoints $\{s_0, ..., s_{n_S}, p_0, .., p_{n_K}\}$ until the total euclidean distance $\mathcal{L}_S^T$ reaches another given parameter λ_T. The computation of $\mathcal{L}_S^T$ follows the Fast Marching procedure with a unit potential as for $\mathcal{L}_S$ but without updating its values at each iteration.

The $\mathcal{U}_S, \mathcal{L}_S$ update step modifies the natural propagation of the front. To correct and update the modified values of the front, a Voronoi index map $\mathcal{V} : \Omega \to \mathbb{N}$, computed in parallel of $\mathcal{U}_S$, is defined for a current set of source points S as

$$\forall x \in \mathcal{R}_j \ , \ \mathcal{V}(x) = j \tag{4}$$

where

$$\mathcal{R}_j = \left\{ x \in \Omega \ , \ \mathcal{U}_{s_j}(x) \leq \mathcal{U}_{s_i}(x) \ , \ \forall i \in \{1, ..., n_S\} \ , \ i \neq j \right\} \tag{5}$$

Every detected keypoint j has its own Voronoi region $\mathcal{R}_j$ containing its closest points according to geodesic distance. When a keypoint is detected, the algorithm continues to update the $\mathcal{U}_S, \mathcal{L}_S$ values in $\mathcal{R}_j$ as detailed in [3].

2.3 Hessian-Based Vascular Enhancement Filtering

A well-known local approximation of a vessel consists in a tube elongated in the direction of the vessel and with a Gaussian profile in its orthogonal plane. Let denote by λ_1, λ_2 with $|\lambda_1| \leq |\lambda_2|$ and v_1, v_2 respectively the two eigenvalues and two eigenvectors of the Hessian matrix at the centre of such 2D tubular structure. One can notice that v_1 is aligned with the direction of the vessel and v_2 with its normal direction, and the eigenvalues verify $|\lambda_1| \ll |\lambda_2|$. The design of an enhancement function or vesselness map $\mathcal{F} : \Omega \to \mathbb{R}$ based on the last property allows to characterize vascular structures in an image. As well summarized in [16], many authors have proposed different variants for $\mathcal{F}$ e.g. Frangi et al. [14]. Very recently, Jerman et al. [16] improved the state of the art methods by designing a more robust enhancement filter. They proposed to regularize λ_2 as follows

$$\lambda_\rho(\sigma) = \begin{cases} \lambda_2 & \text{if } \lambda_2 > \tau \max\limits_{x \in \Omega} \lambda_2(x,\sigma) \\ \tau \max\limits_{x \in \Omega} \lambda_2(x,\sigma) & \text{if } 0 < \lambda_2 \leq \tau \max\limits_{x \in \Omega} \lambda_2(x,\sigma) \\ 0 & \text{otherwise} \end{cases} \tag{6}$$

where $\tau \in [0,1]$ is a threshold parameter and σ is the standard deviation of the Gaussian used to compute the Hessian image. In fact, the Hessian of the image is computed on a Gaussian scale space by convolving I with second derivatives of Gaussian. Then, they defined the scale dependent version of $\mathcal{F}$ by

$$\mathcal{F}_\sigma = \begin{cases} 0 & \text{if } \lambda_2 \leq 0 \text{ or } \lambda_\rho \leq 0 \\ 1 & \text{if } \lambda_2 \geq \lambda_\rho/2 > 0 \\ \lambda_2^2(\lambda_\rho - \lambda_2)\left(\frac{3}{\lambda_2+\lambda_\rho}\right)^3 & \text{otherwise} \end{cases} \tag{7}$$

Finally, $\mathcal{F}$ is obtained for all $x \in \omega$ by

$$\mathcal{F}(x) = \sup\left\{\mathcal{F}_\sigma(x)\ ,\ \sigma_{\min} \leq \sigma \leq \sigma_{\max}\right\}. \tag{8}$$

3 The Proposed Minimal Path Based Framework

3.1 Binary Metric Design

In vessel extraction applications, an isotropic metric is a function of the image value that must assign low values to vessels. On real images like retinal ones, the keypoint detection method (section 2.2) with classical isotropic metric models (as described e.g. in [21, 13]) generally produces many outlier keypoints. Indeed, those simple models only consider pixel intensities without any a priori knowledge on vascular structures leading to false positive detection. Therefore, before solving the minimal path problem, we pre-process the image with a vascular enhancement filter and threshold the obtained vesselness map $\mathcal{F}$ with threshold parameter δ to get a binary mask $\mathcal{F}_\delta$ depicting the segmented vessels. This mask is then used to design a binary metric $\mathcal{P}_b$ as follows: the background is put to infinity in order to stop the front propagation at vessel boundaries, whereas the vascular shape is equipped with a unit metric. This constrains the minimal paths to lie only on vascular patterns without any use of sophisticated stopping criteria and anisotropic models.

The vascular enhancement filter used is the filter introduced by Jerman et al. [16] as described in section 2.3. Figure 1(b) and 1(c) respectively illustrate the problem of false positive keypoints when using an intensity-based metric of the form $\mathcal{P} = \mathcal{P}_0 + |I - c|$ with c an approximate value of the vessel pixels, and the improvement result with the binary metric $\mathcal{P}_b$.

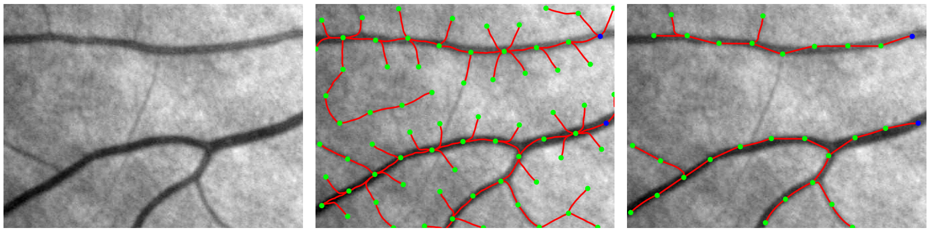

(a) (b) (c)

Fig. 1: (a) Original cropped retinal image. (b) Outlier keypoints with an intensity-based isotropic metric. (c) The proposed solution using an Hessian-based binary metric.

3.2 Centred Keypoint Detection

If we apply the keypoint detection algorithm directly with $\mathcal{P}_b$, some problems may persist. First, the paths are not necessarily centred as observed on Figure 1(c). Secondly, outlier keypoints may appear inside the mask for small values of the parameter λ (see section 2.2) as shown Figure 2 on a synthetic example. Thus, we propose to constrain the MPWKD at the centre of vessels. The algorithm now designates a point p as a keypoint if p satisfies two conditions:

$$\begin{cases} \mathcal{L}_S(p) \geq \lambda \text{ as in 2.2} \\ p \text{ lies on a vessel centreline} \end{cases} .$$

(a) (b)

Fig. 2: Outlier keypoints problem with the MPWKD on a binary metric (left). The proposed solution is on the right.

To check that p lies on a centreline, we compute the skeleton of $\mathcal{P}_b$ and check if p is inside. The skeleton can be approximated for instance by thresholding the gradient magnitude of the distance-to-boundary map $\mathcal{D} : \Omega \to \mathbb{R}_+$

$$\text{Skeleton} = \{x \in \Omega \, , \, \|\nabla \mathcal{D}\| \leq \tau_s\}. \tag{9}$$

Indeed, maxima of $\mathcal{D}$ are reached at centrelines with very small values of $\|\nabla\mathcal{D}\|$. Decreasing τ_s makes the skeleton thinner but too small values may ignore some branches. As explained in [13], to compute $\mathcal{D}$, two different front propagations using the $\mathcal{P}_b$ metric are needed. The first one starts from one source point inside the vascular shape, and because of the infinite background, the front is automatically frozen at vessel boundaries. Then, those boundary points are used as source points in a second front propagation whose resulting geodesic distance map $\mathcal{U}_S$ is exactly the desired distance-to-boundary map $\mathcal{D}$.

Once the keypoint detection has been constrained on the skeleton, no more outlier keypoints should appear. However, the presence of noise on the boundaries of $\mathcal{P}_b$ can induce some errors in the skeleton such as new outlier branches as described in [1]. Fortunately, keypoints are extracted along the skeleton with a quasi constant spacing equal to λ. This avoids to select outlier keypoints close to the boundary by choosing λ greater than typical radius values inside the vascular shape.

Regarding the extracted minimal paths, they still remain not centred. Therefore, similarly to [13], instead of using $\mathcal{P}_b$ we propagate the MPWKD with a new metric function based on $\mathcal{D}$ defined by

$$\mathcal{P}_c = \begin{cases} +\infty & \text{in the background } (\mathcal{P}_b = +\infty) \\ \mathcal{P}_0 + e^{-\alpha\mathcal{D}} & \text{elsewhere } (\mathcal{P}_b = 1) \end{cases} \tag{10}$$

where $\alpha \in \mathbb{R}_+$ controls the exponential. Thus, the lowest metric weights are attributed to centrelines (high values of $\mathcal{D}$) and the extracted minimal paths are constrained to lie on centrelines as well. Figures 3(a)-(g) illustrates the proposed centred keypoint detection method on a synthetic example.

Note that $\mathcal{P}_b$ and $\mathcal{P}_c$ may contain different sets of connected pixels describing the entire vascular structure. In this case, we apply the method with multiple source points arbitrary selected inside each set of pixels.

3.3 Cycles and Graph Representation

An important assumption of the Fast Marching is that $\mathcal{U}_S$ can only increase with the front propagation. As a consequence, if a keypoint p has been already detected and its $\mathcal{U}_S$ value frozen to zero, all the next detected keypoints will be different from p. Thus, the centred MPWKD described in the last section is still unable to extract closed curves. This can be observed on Figures 3(g) and 4(a) where five pairs of keypoints remain unconnected, while the synthetic tubular shape is constituted of five cycles (or loops) needing to be closed.

The problem of detecting cycles in vascular networks is particularly important to characterize specific vascular anomalies encountered for instance in tumours where the excessive formation of new vessels can lead to the apparition of cycles [12]. Therefore, cycles detection must be incorporated in the proposed framework especially for 3D applications, whereas in 2D images some cycles may be caused by the superposition of vessels inducing wrong bifurcations. The problem of 2D wrong bifurcations is not addressed in this study but solutions may be found for instance in [2].

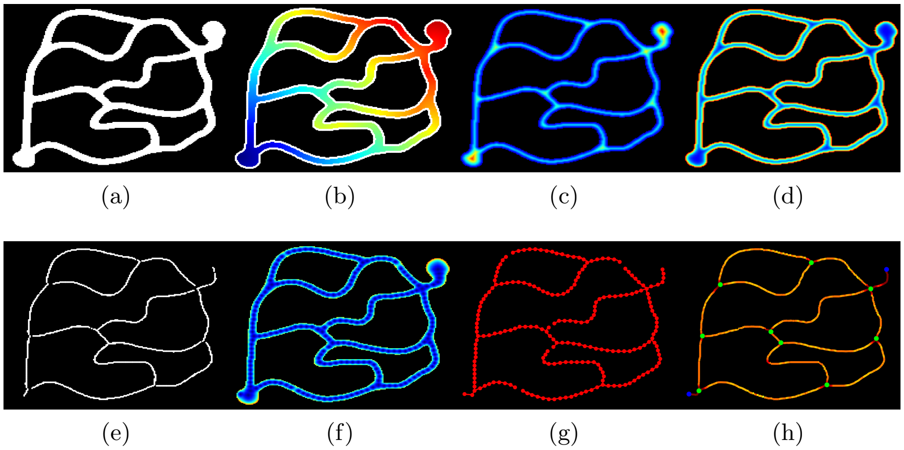
(a) (b) (c) (d)

(e) (f) (g) (h)

Fig. 3: Centred keypoint detection. (a) Original synthetic tubular binary image. (b) Boundaries detection (in white). (c) Distance to boundary map $\mathcal{D}$ (high values in red). (d) $\mathcal{P}_c$ metric. (e) Skeleton. (f) Geodesic distance map $\mathcal{U}_S$ computed by centred keypoint detection. (g) Centred keypoint detection result. (h) Diameters and graph representation (bifurcations and leaves resp. in green and blue)

The notion of cycles leads us to represent vascular networks as graphs with nodes and edges. The keypoint detection method is by construction a tree structure approach where keypoints are the nodes and the extracted minimal paths are edges. When a keypoint p_1 is originated from the keypoint p_0 i.e. the minimal path extracted by the detection of p_1 has reached after gradient descent on $\mathcal{U}_S$ the keypoint p_0, we say that p_0 is the father of p_1, and p_1 the child of p_0. Let notice that a keypoint cannot have more than one father. We also define a leaf by a keypoint that has no child, and a bifurcation by a keypoint with at least two children. A keypoint with only one child is not considered as a node but as a sample point of a minimal path joining two nodes. Regarding source points, they must be carefully treated. With one, two or more than three children, a source point is considered respectively as a leaf, a sample point, or a bifurcation.

On Figure 4(a), we notice that keypoints with missing connections are all leaves. We begin by identifying them. Among all leaves, we keep only pairs of keypoints $\{(s_1, e_1), ..., (s_n, e_n)\}$ (here $n = 5$) whose Voronoi regions have at least one pixel in common, as shown on 4(c). Then, we propagate the Fast Marching with the metric $\mathcal{P}_c$ and the s_i as source points. As soon as a point e_i is reached by the front, the minimal path joining e_i to s_i is extracted by gradient descent on $\mathcal{U}_S$. The front stops to propagate when all the n paths have been extracted. Finally, the n paths are added to their corresponding edges to form a complete graph structure. The obtained result is shown on Figure 3(h) where leaves and bifurcations are respectively coloured in blue and green.

In some cases, two leaves may have their Voronoi Regions side by side but there is no need to connect them. This is for example the case of some close leaves on the synthetic tree Figure 6. To avoid such problems of outlier cycles, we use the criterion introduced by Kaul et al. [17] to treat general closed curves. Let $f(s_i)$ be the father of s_i. We impose to join e_i to s_i only if

$$\left| \|e_i - f(s_i)\| - \|e_i - s_i\| - \lambda \right| \leq \epsilon \tag{11}$$

where $\epsilon/\lambda \sim 0.2$.

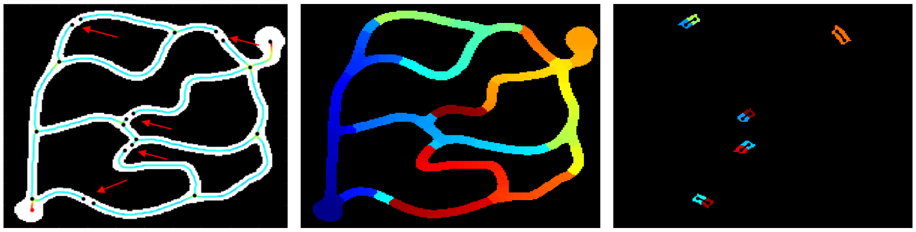
(a) (b) (c)

Fig. 4: Detection and closure of cycles on a synthetic tubular binary image. (a) Centred keypoint detection result. (b) Voronoi index map $\mathcal{V}$ (low indexes in blue, high ones in red). (c) The five pairs of neighbour leaves with their computed connections and Voronoi regions.

3.4 Subpixel Vessel Extraction

Minimal paths γ^* are extracted by gradient descent on $\mathcal{U}_S$ according to the following equation

$$\frac{d\gamma^*(t)}{dt} = -\frac{\nabla \mathcal{U}_S(\gamma^*(t))}{\|\nabla \mathcal{U}_S(\gamma^*(t))\|}. \tag{12}$$

Therefore, the sampling points describing γ^* have subpixel coordinates. This makes the paths more smooth and regular. Nevertheless, in the keypoint detection approach, the computation of $\nabla \mathcal{U}_S$ may induce some errors in the path extraction. Indeed, the paths extraction is done while the map $\mathcal{U}_S$ is not completely computed yet. Thus, some $\mathcal{U}_S$ values have still an infinite value causing troubles in the gradient computation, such as stagnancy of the path before reaching the source illustrated on Figure 5.

To overcome this kind of problems, we modify the classical computation of the gradient to take into account the infinite values of $\mathcal{U}_S$ at boundaries. Let $x \in \mathbb{R}^2$ be a sampling point of γ^*. The gradient $\nabla \mathcal{U}_S(x)$ at x is computed by bilinear interpolation from the 4 pixel neighbours of x. Let $p_{i,j} \in \Omega$ (line i, column j) be a pixel neighbour of x, and $p_{\min}$ the neighbour of $p_{i,j}$ with the smallest $\mathcal{U}_S$

value. If $\mathcal{U}_S(p_{i,j}) = +\infty$, we impose the coordinate of $\nabla\mathcal{U}_S(p_{i,j})$ in the direction of $p_{\min}$ to be 1 and the other coordinate to be 0. Otherwise, we look at the 4 neighbours of $p_{i,j}$. For instance in the vertical direction, if $\mathcal{U}_S(p_{i-1,j}) = +\infty$ or $\mathcal{U}_S(p_{i+1,j}) = +\infty$, then $\partial_x\mathcal{U}_S(p_{i,j})$ is computed respectively by a forward or a backward finite difference; if both $\mathcal{U}_S(p_{i-1,j}) = +\infty$ and $\mathcal{U}_S(p_{i+1,j}) = +\infty$, then $\partial_x\mathcal{U}_S(p_{i,j}) = 0$; otherwise, we use a central finite difference. We do the same in the horizontal direction. At the end, if $\partial_x\mathcal{U}_S(p_{i,j})$ and $\partial_y\mathcal{U}_S(p_{i,j})$ are both very close to zero, we impose to move in the direction of $p_{\min}$ as for the case $\mathcal{U}_S(p_{i,j}) = +\infty$. We repeat this procedure for each neighbour of x and then we can interpolate.

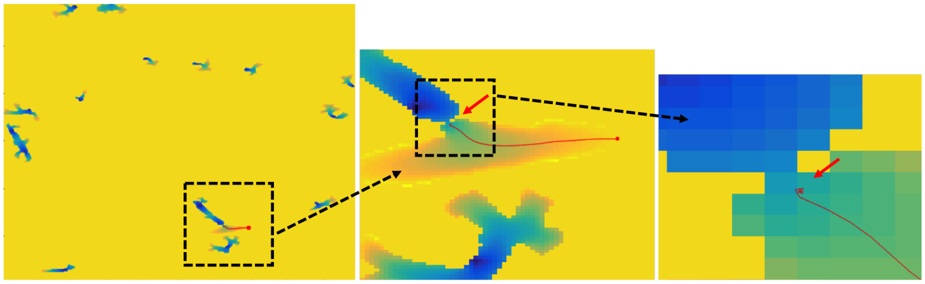

Fig. 5: Stagnation of the gradient descent before reaching the source point on a retinal image example. The path is superimposed on the geodesic distance map $\mathcal{U}_S$ with low and high values respectively in blue and yellow.

3.5 Vessel Diameter Estimation

From the distance-to-boundary map $\mathcal{D}$, we can estimate vessel diameters. At a sample point x belonging to a centred minimal path, the local diameter can be defined by $2\mathcal{D}(x)$. Since minimal paths are subpixel curves whereas $\mathcal{D}$ is a pixel mapping, we interpolate $\mathcal{D}(x)$ by a bilinear interpolation on the 4 pixel neighbours of x. This local diameter estimation is realized for every edge of the extracted graph. Figure 6 illustrates the performance of the proposed framework respectively on a synthetic tree and a cropped retinal image.

4 Experiments on Retinal images

The proposed framework was tested on the DRIVE database [26] composed of 40 retinal images. The database is divided in two sets of 20 images for training and test. For each image, a manual segmentation serves as groundtruth and a mask delineating the FOV (field of view) is also available. For the test set, two manual segmentations are provided.

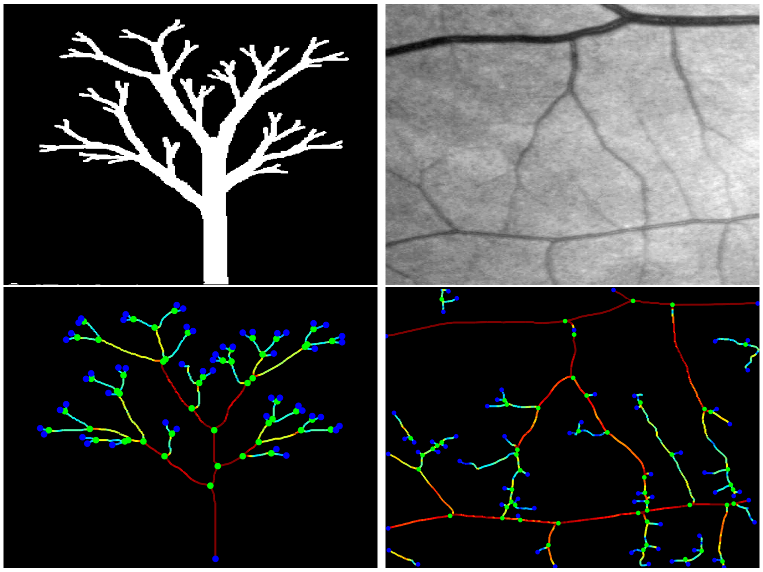

Fig. 6: Illustration of the method on a synthetic tree (left) and a cropped retinal image (right). Top line: original images. Bottom line: our vessel extraction method; high diameters are in yellow/red, low ones in blue/green; bifurcations and leaves are respectively in green and blue.

To evaluate the results, we first measure the accuracy of the segmentation results, i.e. the sum of the true positive and true negative pixels divided by the number of pixels in the FOV. The training set is first used to estimate the optimal values of parameters τ in Equation (6) and δ in Section 3.1. We found $(\tau, \delta) = (0.25, 0.9)$ by maximizing the average accuracy of the training images. The other main parameters are fixed to $\sigma = \{0.1, 0.2, ..., 2.9, 3\}$, $\lambda = 5$, $\mathcal{P}_0 = 0.1$, $\alpha = 0.5$, $\tau_s = 0.5$, $\epsilon = 0.2\lambda$.

For each test image, two segmented images are evaluated. The first one is the thresholded vesselness map $\mathcal{F}_\delta$ introduced by Jerman et al. [16], and the second one is a segmented image reconstructed from vessel centrelines and diameters extracted with the proposed framework. With $\mathcal{F}_\delta$, we evaluate the performance of the vascular enhancement filter used [16]. With the reconstructed image, we evaluate the accuracy of the vessel centrelines and diameters extracted by our method. Figure 7 shows the different segmented images from the test image giving the maximal accuracy.

Results on test images are presented in Table 1. We compare our result with two other methods, Benmansour and Cohen [4] and Chen and Cohen [6], where an anisotropic metric and a one dimension higher numerical scheme for estimation of the diameters are used as detailed in Section 1. Their performance measures were taken from [6]. We used the same experimental conditions: only the second manual segmentations are used as groundtruth and the FOV mask is eroded by 11 pixels to remove the effect of the FOV boundary on $\mathcal{F}_\delta$. With higher maximal and average accuracies than [4] and higher maximal accuracy than [6], we see the pretty good performance of our reconstruction from centrelines demonstrating the quality of our vessel extraction method, even if we used an isotropic metric model and a classical numerical scheme. Also, the advantage of pre-segmenting the images with the Jerman et al. [16] filter is clearly pointed out by its outperformance.

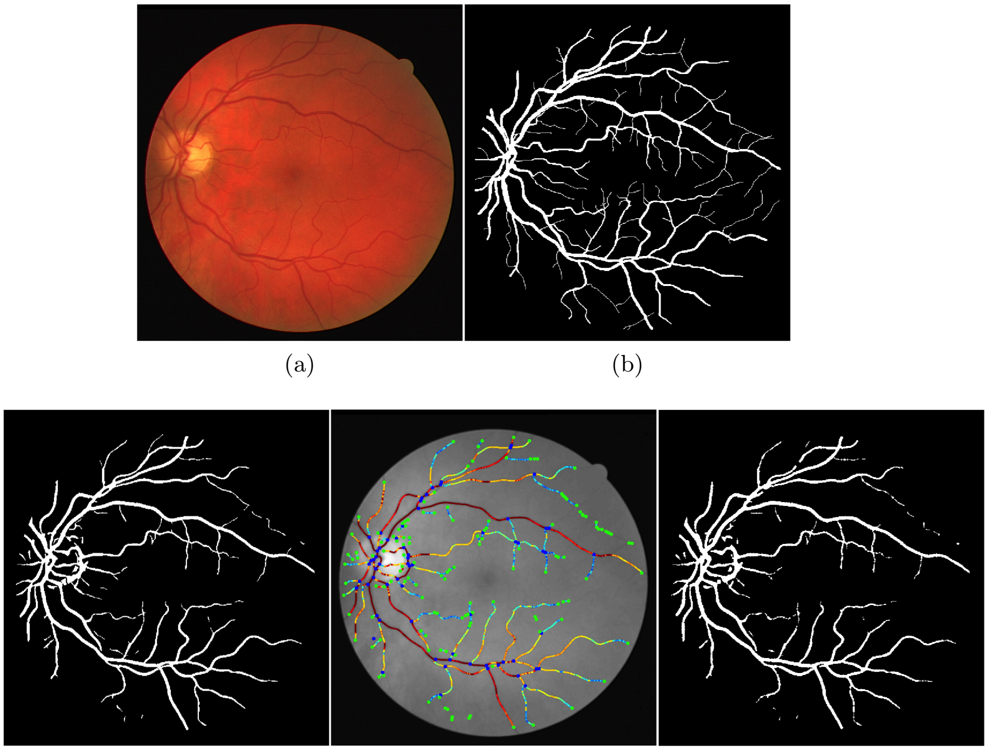

(a) (b)

(c) (d) (e)

Fig. 7: Best result of the proposed framework on the DRIVE test dataset. (a) Original test image. (b) Groundtruth. (c) Thresholded vesselness map $\mathcal{F}_\delta$ with the Hessian-based filter [16]. (d) Centrelines and diameters with the proposed method. (e) Segmented image reconstructed from (d).

Because of the large number of negatives in the background of segmented vessel images, as explained in [25], we usually prefer sensitivity (recall) and precision to measure vessel detection performance. Therefore, we plot on figure 8-left the sensitivity of our results as a function of (1-precision) for all test images. We see how the points corresponding to Jerman and to our reconstruction lie closely to

Table 1: Accuracy measures on the 20 retinal images of the DRIVE test dataset.

Methods	Maximum	Minimum	Average	Standard deviation
Benmansour and Cohen [4]	0.947	0.927	0.9372	0.0054
Chen and Cohen [6]	0.949	0.930	0.9397	0.0052
Jerman et al. [16]	0.954	0.924	0.9410	0.0096
Our reconstruction from centrelines	0.951	0.923	0.9382	0.0089

the first manual segmentations of the DRIVE dataset, except few images with lower sensitivity. We also observe that our centrelines reconstruction algorithm lacks of sensitivity comparing to Jerman. This is due to some unreconstructed small vessel branches. However, its performance remains enough similar to Jerman to ensure that centrelines are pretty well extracted. On figure 8-right, a ROC curve whose points correspond to several values of parameters (τ, δ) applied on the first test image illustrates a performing profile.

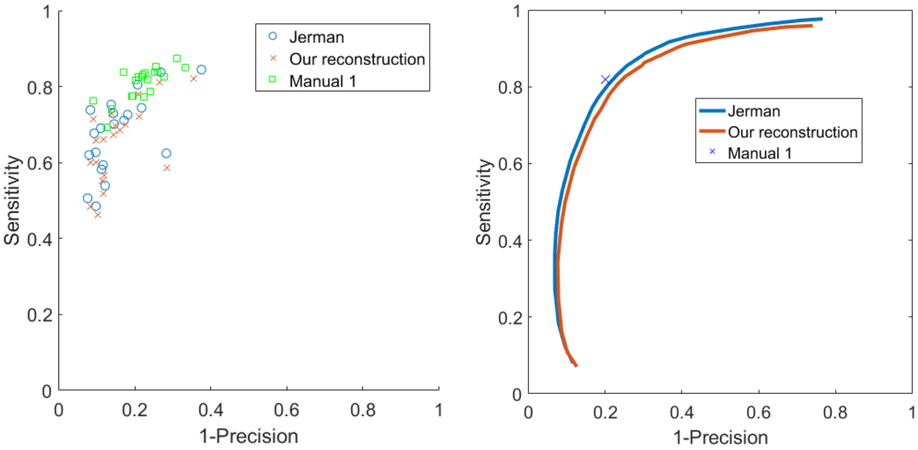

Fig. 8: Sensitivity vs (1-Precision) graph comparing Jerman and our reconstruction to the first manual segmentations of the DRIVE dataset. Left: each point corresponds to one image of the test set. Right: ROC curve of the first test image.

5 Conclusion

In this study, we showed how to design a binary isotropic metric with vascular a priori knowledge and introduced a new centred keypoint detection method to accurately extract centrelines, diameters and bifurcations of a vascular network.

This framework has the advantage to use the classical minimal path based methods and in the same time to produce performance being similar even better to the recent methods as shown on the retinal images DRIVE database. Besides, it can easily be extended to 3D. As future works, the robustness of the proposed graph description of vascular networks to outlier bifurcations and outlier cycles should be studied. Also, the proposed framework will be applied on 3D ultrasensitive Doppler images to improve our recent results presented in [8].

6 Acknowledgement

We would like to particularly thank Dr. Da Chen for his precious help and advice.

References

1. Attali, D., Boissonnat, J.D., Edelsbrunner, H.: Stability and computation of medial axes-a state-of-the-art report. In: Mathematical foundations of scientific visualization, computer graphics, and massive data exploration, pp. 109–125. Springer (2009)
2. Bekkers, E.J., Duits, R., Mashtakov, A., Sanguinetti, G.R.: Data-driven subriemannian geodesics in se (2). In: International Conference on Scale Space and Variational Methods in Computer Vision. pp. 613–625. Springer (2015)
3. Benmansour, F., Cohen, L.D.: Fast object segmentation by growing minimal paths from a single point on 2d or 3d images. Journal of Mathematical Imaging and Vision 33(2), 209–221 (2009)
4. Benmansour, F., Cohen, L.D.: Tubular structure segmentation based on minimal path method and anisotropic enhancement. International Journal of Computer Vision 92(2), 192–210 (2011)
5. Bullitt, E., Gerig, G., Pizer, S.M., Lin, W., Aylward, S.R.: Measuring tortuosity of the intracerebral vasculature from mra images. IEEE transactions on medical imaging 22(9), 1163–1171 (2003)
6. Chen, D., Cohen, L.D.: Piecewise geodesics for vessel centerline extraction and boundary delineation with application to retina segmentation. In: International Conference on Scale Space and Variational Methods in Computer Vision. pp. 270–281. Springer (2015)
7. Chen, D., Mirebeau, J.M., Cohen, L.D.: Vessel tree extraction using radius-lifted keypoints searching scheme and anisotropic fast marching method. Journal of Algorithms & Computational Technology 10(4), 224–234 (2016)
8. Cohen, E., Deffieux, T., Demené, C., Cohen, L.D., Mickael, T.: 3d vessel extraction in the rat brain from ultrasensitive doppler images. In: CMBBE 2016 (2016)
9. Cohen, E., Deffieux, T., Tiran, E., Demene, C., Cohen, L., Tanter, M.: Ultrasensitive doppler based neuronavigation system for preclinical brain imaging applications. In: Ultrasonics Symposium (IUS), 2016 IEEE International. pp. 1–4. IEEE (2016)
10. Cohen, L.D., Kimmel, R.: Global minimum for active contour models: A minimal path approach. International journal of computer vision 24(1), 57–78 (1997)
11. Crandall, M.G., Lions, P.L.: Viscosity solutions of hamilton-jacobi equations. Transactions of the American Mathematical Society 277(1), 1–42 (1983)

12. Demené, C.: Cartographie vasculaire et fonctionnelle du cerveau par échographie Doppler ultrarapide chez le petit animal et le nouveau-né. Ph.D. thesis, Paris 7 (2015)
13. Deschamps, T., Cohen, L.D.: Fast extraction of minimal paths in 3d images and applications to virtual endoscopy. Medical image analysis 5(4), 281–299 (2001)
14. Frangi, A.F., Niessen, W.J., Vincken, K.L., Viergever, M.A.: Multiscale vessel enhancement filtering. In: International Conference on Medical Image Computing and Computer-Assisted Intervention. pp. 130–137. Springer (1998)
15. Hart, W.E., Goldbaum, M., Côté, B., Kube, P., Nelson, M.R.: Measurement and classification of retinal vascular tortuosity. International journal of medical informatics 53(2), 239–252 (1999)
16. Jerman, T., Pernus, F., Likar, B., Spiclin, Z.: Enhancement of vascular structures in 3d and 2d angiographic images. IEEE transactions on medical imaging 35(9), 2107 (2016)
17. Kaul, V., Yezzi, A., Tsai, Y.: Detecting curves with unknown endpoints and arbitrary topology using minimal paths. IEEE Transactions on Pattern Analysis and Machine Intelligence 34(10), 1952–1965 (2012)
18. Law, M.W., Chung, A.C.: Three dimensional curvilinear structure detection using optimally oriented flux. In: European conference on computer vision. pp. 368–382. Springer (2008)
19. Li, H., Yezzi, A., Cohen, L.: 3d multi-branch tubular surface and centerline extraction with 4d iterative key points. Medical Image Computing and Computer-Assisted Intervention–MICCAI 2009 pp. 1042–1050 (2009)
20. Mirebeau, J.M.: Anisotropic fast-marching on cartesian grids using lattice basis reduction. SIAM Journal on Numerical Analysis 52(4), 1573–1599 (2014)
21. Peyré, G., Péchaud, M., Keriven, R., Cohen, L.D.: Geodesic methods in computer vision and graphics. Foundations and Trends® in Computer Graphics and Vision 5(3–4), 197–397 (2010)
22. Rouy, E., Tourin, A.: A viscosity solutions approach to shape-from-shading. SIAM Journal on Numerical Analysis 29(3), 867–884 (1992)
23. Sethian, J.A.: A fast marching level set method for monotonically advancing fronts. Proceedings of the National Academy of Sciences 93(4), 1591–1595 (1996)
24. Sethian, J.A.: Level set methods and fast marching methods: evolving interfaces in computational geometry, fluid mechanics, computer vision, and materials science, vol. 3. Cambridge university press (1999)
25. Sofka, M., Stewart, C.V.: Retinal vessel centerline extraction using multiscale matched filters, confidence and edge measures. IEEE transactions on medical imaging 25(12), 1531–1546 (2006)
26. Staal, J., Abramoff, M., Niemeijer, M., Viergever, M., van Ginneken, B.: Ridge based vessel segmentation in color images of the retina. IEEE Transactions on Medical Imaging 23(4), 501–509 (2004)
27. Tsitsiklis, J.N.: Efficient algorithms for globally optimal trajectories. IEEE Transactions on Automatic Control 40(9), 1528–1538 (1995)